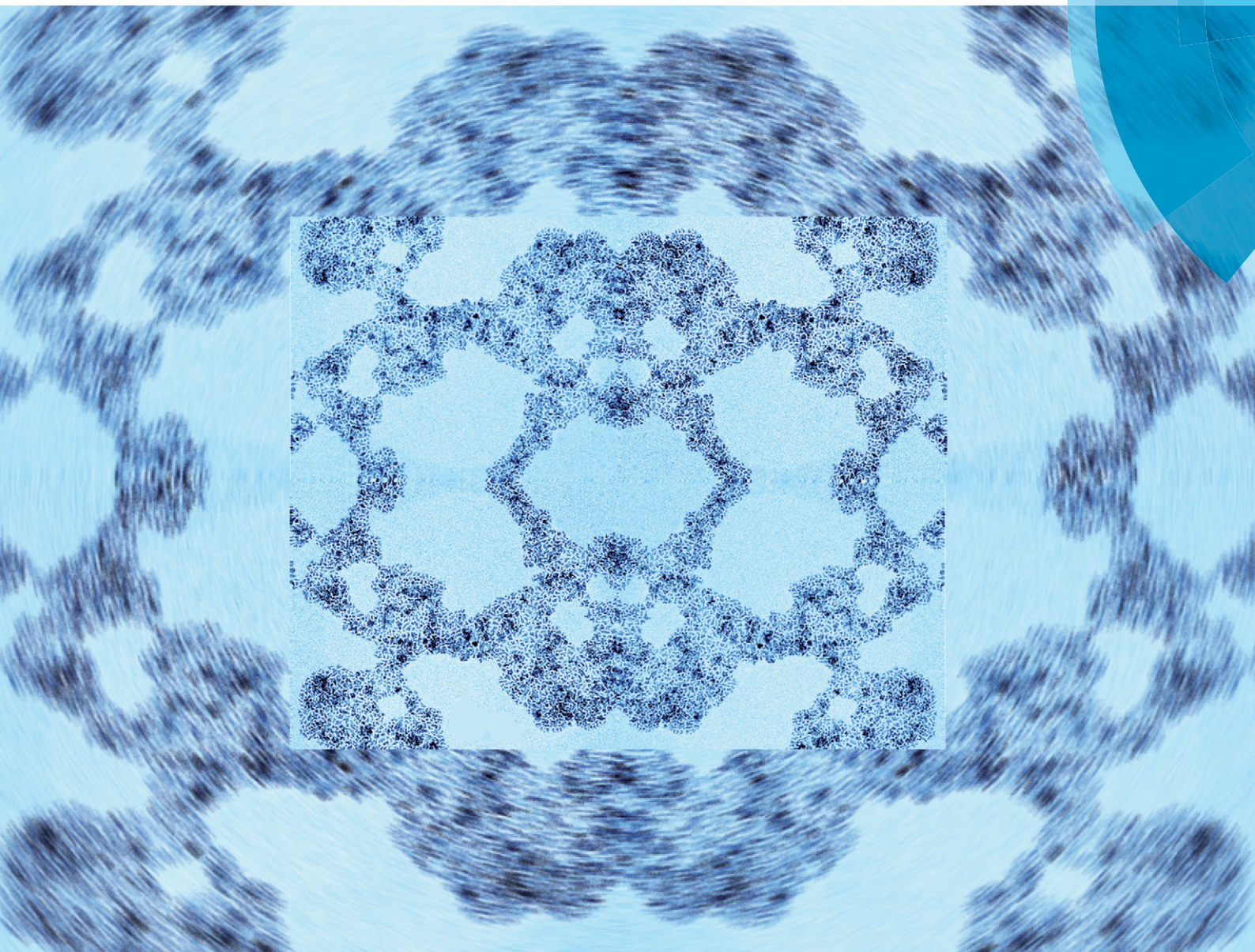


# CrystEngComm

rsc.li/crystengcomm



**PAPER**

Francesca Tana, Andrea Serafini *et al.*  
Particle anisotropy and crystalline phase transition in one-pot synthesis of nano-zirconia: a causal relationship



Cite this: *CrystEngComm*, 2018, 20, 879

## Particle anisotropy and crystalline phase transition in one-pot synthesis of nano-zirconia: a causal relationship†

Francesca Tana,<sup>a</sup>  <sup>\*a</sup> Andrea Serafini,<sup>\*a</sup> Luca Lutterotti,<sup>b</sup> Alberto Cigada,<sup>a</sup> Fabio Variola,<sup>c</sup> Federica Bondioli<sup>d</sup> and Luigi De Nardo  <sup>a</sup>

Crystalline phase evolution and morphological changes are strictly correlated phenomena during the growth of zirconia nanoparticles. In this work, the effects of synthetic variables, reaction time (up to 24 hours) and precursor concentration (0.16 and 0.5 M), of a one-step non-hydrolytic sol-gel route to zirconia are investigated. Zirconium tetrachloride ( $ZrCl_4$ ) is chosen as a zirconium oxide precursor to react in benzyl alcohol. At a low precursor concentration and a short reaction time, pseudo-spherical particles of size 2 nm with a narrow size distribution are observed by transmission electron microscopy (TEM). At this stage, mainly the tetragonal phase is detected. By increasing both the zirconium precursor concentration and reaction time, a broadening of size distribution is observed resulting from the growth of anisotropic particles. Concurrently, an increasing amount of the monoclinic is detected by X-ray diffraction and Raman spectroscopy. As a novelty, Rietveld investigations on electron diffraction ring patterns obtained by transmission electron microscopy are performed. This procedure allows the collection of comprehensive information about nanostructured particles in one-step analysis. The results derived from this analysis, together with the high resolution transmission electron microscopy (HR-TEM) data, consistently support the structural transition from pseudo-spherical tetragonal particles to rice-shaped monoclinic particles.

Received 9th November 2017,  
Accepted 15th December 2017

DOI: 10.1039/c7ce01949a

rsc.li/crystengcomm

### 1. Introduction

Controlled synthesis of crystalline materials, with tunable physicochemical properties and tailor-made topographical features in the nano-range, has been a fascinating objective in numerous branches of modern materials science, since the structural characteristics of nanocrystals directly determine the overall performance. For example, the optical properties of anisotropic metal particles were employed in imaging<sup>1</sup> and for catalysis<sup>2</sup> applications, capitalizing on their tunable efficiency which depends on the surface-to-volume ratio and on the exposed crystal facet, among others.<sup>3</sup> Moreover, the unique size- and shape-dependent optical properties of gold nanoparticles have been used for selective and sensitive detec-

tion of different analytes in bioanalysis<sup>4</sup> or for environmental applications.<sup>5</sup>

Among metal oxides, zirconia ( $ZrO_2$ ) is an important ceramic material that has become an essential constituent in various technological fields. For instance, spherical  $ZrO_2$  nanocrystals have been applied as fuel cell electrolytes, oxygen sensors, and gate dielectrics,<sup>6</sup> while zirconia nanorods were exploited for humidity sensing.<sup>7</sup> Moreover, zirconia nanocrystals with an anisotropic morphology (e.g., rods or rice-shaped),<sup>8,9</sup> are poised to provide new opportunities in the fabrication of fibers, films, ceramic coatings, and grain-oriented ceramics.<sup>10</sup> Furthermore, the phase-dependent optical, conductive and mechanical properties of  $ZrO_2$ <sup>11</sup> were also exploited in sensing application, catalysis, photonics and biotechnology.<sup>12</sup> In this context, monoclinic  $ZrO_2$  is demonstrated to be an effective catalyst<sup>13</sup> and a bioactive coating to improve the osseointegration of biomedical implants,<sup>14</sup> while tetragonal and cubic  $ZrO_2$  are well known phase-transformation-toughened structural materials<sup>15</sup> and represent promising candidates for oxygen sensors.<sup>16</sup>

Different metastable nanometric structures can be stabilized without the addition of dopants or the constriction by a matrix in the synthesis of nanomaterials.<sup>17</sup> The occurrence of metastable tetragonal and cubic phases under ambient conditions in nanocrystalline  $ZrO_2$  systems represents a typical

<sup>a</sup> Department of Chemistry, Materials, and Chemical Engineering "G. Natta", Politecnico di Milano, Via Mancinelli 7, 20131 Milano (MI), Italy.

E-mail: francesca.tana@polimi.it

<sup>b</sup> Department of Materials Engineering, University of Trento, Via Mesiano 77, 38123 Trento (TN), Italy

<sup>c</sup> Department of Mechanical Engineering, University of Ottawa, Ottawa, Ontario, Canada

<sup>d</sup> Department of Industrial Engineering, University of Parma, Parco Area delle Scienze 181/A, 43124 Parma (PR), Italy

† Electronic supplementary information (ESI) available. See DOI: 10.1039/c7ce01949a

example.<sup>18</sup> In this context, the evolution of the zirconia phase in relation to a specific particle size was previously studied, and in particular, the stabilization of the tetragonal phase under environmental conditions was correlated with a critical grain size.<sup>19,20</sup>

A wide variety of synthetic methodologies has been reported for ZrO<sub>2</sub>, including emulsion systems (*i.e.* micro-emulsion, reverse emulsion, and emulsion precipitation methods),<sup>21</sup> the sol-gel route,<sup>22</sup> the microwave technique,<sup>23,24</sup> the hydrothermal/solvothermal method,<sup>10</sup> the surfactant assisted synthesis<sup>25</sup> and the non-hydrolytic sol-gel route.<sup>26,27</sup> Among zirconium precursors, zirconium chloride was successfully used to obtain ZrO<sub>2</sub>, exploiting different synthetic procedures.<sup>28–30</sup>

Generally, materials resulting from low temperature processes (*e.g.* sol-gel or precipitation method derived powders) are amorphous, making their physicochemical properties (*e.g.* particles size, size distribution, and purity) difficult to control through the modulation of the experimental parameters. In parallel, structural changes to a crystalline phase can be induced by thermal treatments,<sup>31</sup> as well as *via* nanoparticle agglomeration phenomena. In the specific case of zirconia, the one-step synthesis of pure phase crystals was also achieved through wet methods (*e.g.* hydrothermal/solvothermal processes), which are often supported by suitable capping agents,<sup>9,25,32,33</sup> or by the non-aqueous sol-gel route.<sup>26,27</sup> The addition of an appropriate capping agent/surfactant results in a modification of the surface energy of growing particles and enables, in principle, the control over particle size distribution and morphology.

The non-aqueous sol-gel route capitalizes on the possibility of obtaining crystalline nanopowders by controlling the reaction rate through the non-hydrolytic condensation reaction between a metal halide and a metal alkoxide in an appropriate solvent.<sup>34–36</sup> Among oxygen donor solvents employed for this procedure,<sup>37,38</sup> benzyl alcohol was proved to be a versatile reaction medium for the synthesis of many metal oxides, involving one precursor species and a solvent.<sup>35</sup> This allows to obtain particles with an available, non capped, surface, further avoiding the use of potential hazardous surfactants. Moreover, avoiding the use of templates, a reduced amount of impurities is achieved in the final product.

Notably, the impact of the crystalline structure connected with specific particle geometry still needs to be fully elucidated. In fact, despite the advantages of these methods, the simultaneous control of size, geometry and crystallinity of ZrO<sub>2</sub> nanoparticles still poses significant challenges. Therefore, envisioning new synthetic approaches to precisely control and fine tune nanoparticle properties has become a priority in the field of ceramic materials.

Deep comprehension of the mechanisms involved in crystal growth, which often can be hardly obtained from a specific experimental set-up, goes along with the development of suitable characterization techniques. The implementation of crystal characterization is indeed nowadays increasingly necessary to enable the preparation of highly controlled nano-

structures for more specific applications. The collection of comprehensive information about nanostructured particles in one-step analysis, such as the Rietveld method applied to TEM electron diffraction ring patterns,<sup>39</sup> represents a relevant opportunity in terms of both the time and sample requirement. Nowadays, indeed, determination of the size, shape and crystalline phase of polymorphic nanopowders generally relies on different techniques.

In this work, we present a comprehensive investigation of the synthesis and evolution of zirconia nanoparticles by a non-hydrolytic sol-gel route. The effects of experimental variables on crystal growth were investigated by rationally modulating the reaction time and precursor concentration. The variation of the experimental conditions allowed the control of the phase and structural evolution of the final powders without the addition of template/capping agents or mineralizing agents. The results obtained from conventional characterization techniques, such as X-ray diffraction (XRD), Raman spectroscopy, and transmission electron microscopy (TEM), were compared with those obtained from Rietveld analysis applied to electron diffraction ring patterns acquired by TEM.

## 2. Experimental section

### 2.1 Chemicals

Zirconium(IV) tetrachloride (ZrCl<sub>4</sub>) was supplied by ABCR (Germany). Tetrahydrofuran (THF), ethanol and benzyl alcohol (BzOH) were purchased from Sigma Aldrich. All chemicals were used as received without any further purification.

### 2.2 Synthesis of zirconia nanoparticles

According to a previously reported protocol,<sup>27</sup> zirconium(IV) tetrachloride (ZrCl<sub>4</sub>) solutions in benzyl alcohol (BzOH) were prepared at different concentrations (0.16 and 0.5 M) under continuous stirring. In order to obtain reaction mixtures at different concentrations, a given quantity of ZrCl<sub>4</sub> was added into two different glass tubes containing 5 ml of BzOH each, under vigorous stirring at room temperature. After 15 minutes, the solutions were heated to 200 °C in an oil bath. For each concentration, three different heating times were selected: 2.5, 7 and 24 hours. The resulting samples were progressively named *xZ<sub>y</sub>*, where *x* represents the molar concentration of the zirconium precursor in solution and *y* the reaction time, thereby determining the following labels to identify different samples: 0.16Z<sub>2.5</sub>, 0.16Z<sub>7</sub>, 0.16Z<sub>24</sub>, 0.5Z<sub>2.5</sub>, 0.5Z<sub>7</sub>, and 0.5Z<sub>24</sub>.

After the reaction termination, the resulting suspensions were centrifuged four times for 15 min at 4000 rpm, with the addition of THF, in order to remove reaction byproducts. The powders were then centrifuged one more time in ethanol. Finally, the wet powders were allowed to dry in open air. The purified nanoparticles were used for structural and morphological characterization without any size sorting.

### 2.3 Characterization of zirconia powder

The phase evolution of the synthesized powders was monitored by X-ray diffractometry (XRD, Philips PW 1830) using a Bragg Brentano diffractometer and Cu-K $\alpha_1$  radiation ( $\lambda = 0.154056$  nm). The X-ray diffraction patterns were collected at room temperature in the 10–70°  $2\theta$  range with a scan step size of 0.02°.

An Alpha 300 confocal Raman microscope (WITec, Germany) equipped with a 50 mW 532 nm Nd:YAG laser was used to carry out the Raman analysis of the powders. Each spectrum was collected with 60 second integration time and 7 acquisitions in order to enhance the signal-to-noise ratio. Raman data were processed with the OriginPro software (OriginLab corporation, United States).

Transmission electron microscopy (TEM), high resolution TEM (HR-TEM) and selected area electron diffraction (SAED) measurements were carried out *via* a Philips CM 200 transmission electron microscope operating at 200 kV and equipped with a field emission gun filament. The zirconia nanopowder samples were ultrasonically suspended in ethanol, and a drop of this suspension was deposited onto a 200 mesh holey carbon-coated copper grid. A Gatan US 1000 CCD camera was used and 2048  $\times$  2048 pixel images with 256 gray levels were taken. During the acquisition of the TEM and HRTEM images, the samples did not undergo structural transformation. The analysis was carried out with low beam current densities and short acquisition times in order to prevent the structural transformations induced by the experimental technique. Image analyses of the Bright Field TEM (BF-TEM) micrographs were performed using the ImageJ software,<sup>40</sup> which permitted estimation of the dimension and morphology of nano-sized particles, as well as their statistical distribution. In particular, the mean values and widths of the statistical asymmetric distribution ( $\sigma^-$ ,  $\sigma^+$ ) of nanoparticle dimension were evaluated by fitting the experimental values with a log-normal function. The fast Fourier transform (FFT) pattern of the HR-TEM images was used to assess interplanar distances. These parameters were determined using the Gatan Digital Micrograph® software with an accuracy of  $\pm 1\%$ . The Rietveld analysis of the SAED patterns was carried out using the MAUD program,<sup>39</sup> with electron atomic scattering factors from Peng *et al.*,<sup>41</sup> and *R*-factors for each refinement were reported alongside. Intensity integration along the Debye rings of the nanopowder SAED pattern was performed using the ImageJ plug-in implemented directly in MAUD, which allows the import of two-dimensional diffraction data coming from the TEM camera or imaging-plate detectors directly, preserving the original image of the coordinate position for each data point.<sup>42–44</sup> By using an adequate number of diffraction rings, it was possible to correct for possible tilting errors and center displacement directly in the Rietveld refinement.<sup>44</sup> Intensity profiles were obtained summing up all the azimuthal plots (corresponding to a full integration along the Debye–Scherrer rings). The SAED patterns were acquired with a beam stopper inserted to reduce the intensity

of the transmitted beam. This masked portion of the image was removed and not considered in data modeling. The background of the diffraction pattern was fitted by a polynomial function and an additional Gaussian peak at 0 Q, in order to model the strong low angle signal rise, mainly due to the transmitted beam. In the spectra where a significant contribution from the supporting continuous carbon layer was observed, another two Gaussian peaks were added at 2.97 and 5.55 Q for modeling the contribution to the intensity profile.<sup>45</sup> For the microstructural characterization of crystalline domain size and shape, the instrumental broadening function was determined following the method proposed by Boullay *et al.*<sup>46</sup>

### 3. Results

Representative XRD patterns of completely dried powders prepared with different concentrations of the zirconium precursor at increasing reaction time are shown in Fig. 1.

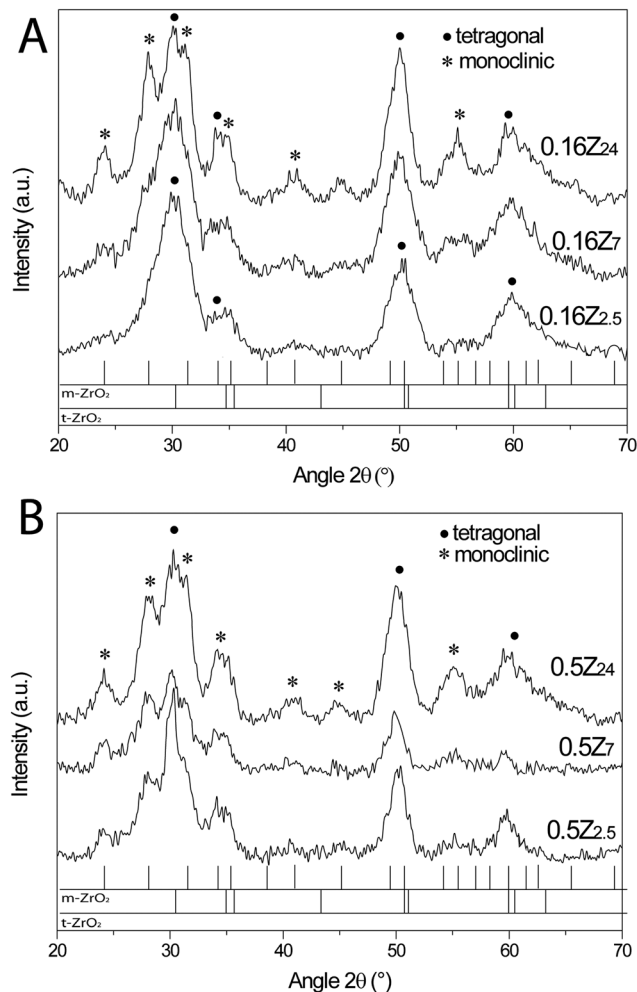


Fig. 1 Representative XRD patterns of the powders prepared at different reaction times (2.5, 7 and 24 hours) with an increasing concentration of the zirconium precursor: (A) 0.16 M and (B) 0.5 M. Reference peaks of monoclinic and tetragonal zirconia, 01-0750 and 50-1089 JPCDS files respectively, are shown at the bottom.

The broad and weak diffraction peaks were associated with fine grains, as previously reported for a non-hydrolytic sol-gel synthesis.<sup>26</sup> Despite the considerable peak broadening, it was nonetheless possible to attribute the diffraction lines to the tetragonal phase of zirconia.<sup>27</sup> In all samples, 0.16Z<sub>2.5</sub>, 0.16Z<sub>7</sub>, 0.16Z<sub>24</sub>, 0.5Z<sub>2.5</sub>, 0.5Z<sub>7</sub>, and 0.5Z<sub>24</sub>, the main visible line of t-ZrO<sub>2</sub> was centered at  $2\theta = 30.3^\circ$  and was assigned to the (011)<sub>t</sub> peak (50-1089 JPCDS file). The additional lines at  $2\theta = 24.1^\circ$ ,  $27.9^\circ$ ,  $31.4^\circ$ ,  $40.8^\circ$  and  $45.1^\circ$ , which were particularly distinguishable after 24 hours of reaction, were assigned to the (110)<sub>m</sub>, ( $\bar{1}11$ )<sub>m</sub>, (111)<sub>m</sub>, (102)<sub>m</sub>, and (211)<sub>m</sub> peaks of m-ZrO<sub>2</sub> (01-0750 JPCDS file).

XRD data showed a similar trend in phase evolution, as a function of time, for the samples prepared at different precursor concentrations. As the reaction time increased, the contribution of the monoclinic phase became more evident. At the shortest reaction time (*i.e.* 2.5 hours), broad peaks attributable to a tetragonal phase were detected in the 0.16Z<sub>2.5</sub> powders. The presence of the monoclinic structure was observed with increasing reaction time from 2.5 to 24 hours, as detected in the 0.16Z<sub>24</sub> sample (Fig. 1A). Such a phase evolution was similarly observed in the 0.5 M samples. Interestingly, for the more concentrated precursor solution, the signals at  $2\theta = 24.1^\circ$  and  $27.6^\circ$  of m-ZrO<sub>2</sub> could be clearly identified as independent peaks after 2.5 hours (Fig. 1B, 0.5Z<sub>2.5</sub> sample). Conversely, monoclinic peaks were only detected as shoulders of the main tetragonal peak centered at  $30.3^\circ$  in both the 0.16Z<sub>2.5</sub> and 0.16Z<sub>7</sub> samples. It thus follows that the tetragonal-to-monoclinic transformation appeared to be faster in more concentrated samples. Nevertheless, no sample showed a pure monoclinic phase, even at the highest concentration/reaction time considered in this study. Moreover, by increasing both reaction time and concentration of the ZrCl<sub>4</sub> precursor in BzOH, the XRD pattern displayed narrower peaks, a result which is most likely associated with the increase in the ZrO<sub>2</sub> nanocrystallite size.

The phase evolution was also investigated by Raman spectroscopy, a technique that permitted the unique identification of cubic and tetragonal zirconia.<sup>27</sup>

Fig. 2 shows the representative Raman spectra of the synthesized powders to visualize the tetragonal-to-monoclinic phase evolution. After 2.5 hours of reaction, the bands at  $\sim 146\text{ cm}^{-1}$ ,  $\sim 261\text{ cm}^{-1}$ ,  $\sim 315\text{ cm}^{-1}$ ,  $\sim 460\text{ cm}^{-1}$  and  $\sim 640\text{ cm}^{-1}$ , characteristic of the t-ZrO<sub>2</sub> phase, were identified.<sup>47</sup> The tetragonal phase belongs to the  $P4_2/nmc$  ( $D_{4h}^{15}$ ) space groups and is expected to exhibit 6 ( $A_{1g} + 2B_{1g} + 3E_g$ ) characteristic bands according to the symmetry space groups and based on the determinative rule of the Raman-active mode.<sup>48</sup> In addition to the t-ZrO<sub>2</sub> Raman signal, a distinguishable band centered in the 180–190  $\text{cm}^{-1}$  range was observed in the 0.5Z<sub>2.5</sub> sample (Fig. 2B). This represents the unresolved doublet at  $\sim 180\text{ cm}^{-1}$  and  $\sim 188\text{ cm}^{-1}$ , a characteristic of m-ZrO<sub>2</sub>.<sup>48</sup> The more complex monoclinic structure, belonging to the  $P2_1$  ( $C_{2h}^5$ ) space groups, gives rise to 18 ( $9A_{1g} + 9B_{1g}$ ) characteristic bands.<sup>48</sup> As the reaction time increased from 7 to 24 hours, the intensity of the monoclinic doublet increased for both the 0.16Z<sub>7</sub> and 0.5Z<sub>7</sub> samples, which became

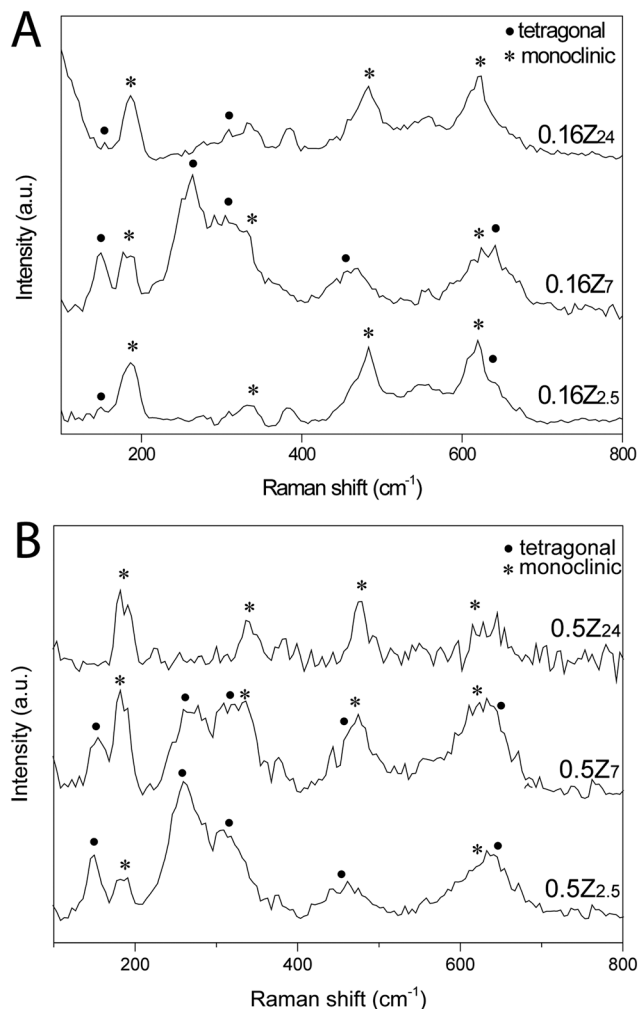


Fig. 2 Representative Raman spectra of the (A) 0.16 M and (B) 0.5 M samples (16Z<sub>2.5</sub>, 0.16Z<sub>7</sub>, 0.16Z<sub>24</sub>, 0.5Z<sub>2.5</sub>, 0.5Z<sub>7</sub>, and 0.5Z<sub>24</sub>), at different reaction times (2.5, 7 and 24 hours).

predominant after 24 hours for the 0.16Z<sub>24</sub> and 0.5Z<sub>24</sub> powders (Fig. 2). For these samples, a number of new m-ZrO<sub>2</sub> bands were detected at 223, 234, 333, 345, 475, 618 and 634  $\text{cm}^{-1}$ ,<sup>47–49</sup> which only appeared as shoulders of the main t-ZrO<sub>2</sub> signals of the zirconia samples reacted for less than 24 hours. The observed higher intensity of the monoclinic peak for the 0.16Z<sub>2.5</sub> sample in comparison with its corresponding XRD spectrum can be explained by considering the presence of broad diffraction XRD peaks that may hide the contribution of the monoclinic phase.

Therefore, in accordance with XRD data, the monoclinic and tetragonal phases were found to coexist in the synthesized samples after 7 hours of reaction. In parallel, the Raman results indicated an unlikely occurrence of pure tetragonal phase, even at 2.5 hours. Some variations in the phase composition observed by XRD and Raman analysis may be attributed to differences in the probed area and depth.<sup>50</sup>

In agreement with the Raman and XRD results, both the monoclinic and tetragonal phases were identified by HR-TEM measurements within the samples (Fig. 3).

The left side of Fig. 3 shows a typical t-ZrO<sub>2</sub> particle image along the [010] direction, displaying the indexed FFT pattern of the particle image (upper inset) and the filtered image (lower inset) obtained *via* inverse Fourier transformation after background subtraction and central spot removal from the FFT pattern. The interplanar distances are 0.295 nm and 0.257 nm, attributable to the t-ZrO<sub>2</sub> *d*-spacings *d*<sub>101</sub> and *d*<sub>002</sub>, respectively. Similarly, the right side of Fig. 3 shows a typical m-ZrO<sub>2</sub> particle, the indexed FFT pattern and the filtered image. The measured interplanar distance of 0.279 nm was attributable to the *d*<sub>111</sub> characteristic *d*-spacing of the m-ZrO<sub>2</sub> phase. Interestingly, the tetragonal lattice was predominantly observed in pseudo-spherical particles (Fig. 3 left), while monoclinic in elongated ones (Fig. 3 right). In order to explore the morphological and microstructural phase evolution of the zirconia powders synthesized under different experimental conditions, conventional TEM imaging was combined with selected area electron diffraction (SAED) measurement. The SAED patterns of the nanocrystal assembly usually exhibit ring patterns analogous to those from powder XRD, hereafter named electron powder diffraction (EPD) patterns. Recently, several works have shown the potential of the Rietveld method applied to the characterization of nanostructured crystalline samples using SAED data.<sup>46,52,53</sup> The proposed route could be profitably employed in place of traditional XRD Rietveld analysis in the case of a limited amount of samples and XRD spectra with poor signal-to-noise ratio.

Since the acquired XRD spectra showed broad and weak peaks, we selected this method for the zirconia nanostructured powders (results shown in Fig. 4) to further investigate the crystalline domain size and shape of the polymorph phases – information that cannot be obtained from TEM micrographs.<sup>53</sup> The EPD pattern of the ZrO<sub>2</sub> particles synthesized at a low precursor concentration and a short reaction time (Fig. 4A) exhibited broad rings. Their positions and widths were best fitted by a bi-phasic system composed of tetragonal and monoclinic crystallites: the former with a pseudo-spherical shape and an average diameter size of 2.3 nm (Fig. 4A), while the latter with a flat ellipsoid shape with

a main axis dimension of 1.6 nm, 2.3 nm and 2.6 nm (Fig. 4A). These findings were in good agreement with the results of the dimensional analysis of the nanoparticles observed in the TEM micrographs (Fig. 5). The dimensional distribution graphs in the insets highlight the presence of pseudo-spherical particles with a narrow size distribution of approximately 2 nm for the 0.16Z<sub>2.5</sub> sample and the growth of slightly elongated particles for the 0.16Z<sub>24</sub>, 0.5Z<sub>2.5</sub>, and 0.5Z<sub>24</sub> samples. Some aggregates in Fig. 5 are visible due to sample preparation for TEM analysis (*i.e.* deposition of the particle suspension followed by drying on the TEM grid).

Only the EPD rings belonging to the monoclinic phase become narrower with increasing precursor concentration at a specific reaction time; the best fitting for this phase was obtained with a pseudo flat ellipsoid shape with average dimensions of the main axes of 2.1 nm, 3.2 nm and 4.9 nm (Fig. 4B), whereas no change in shape and size was observed for the tetragonal phase. The monoclinic nanoparticle broadening was also confirmed by the TEM analysis (Fig. 5); in addition to the pseudo-spherical particles, we observed the presence of elongated rice-shaped particles that well retrace the size and the shape obtained from the Rietveld analysis of the EPD pattern. The same phenomenon, with similar results for both phases, was observed by increasing the reaction time at a fixed concentration (Fig. 4C and 5C). In a similar fashion, at a higher precursor concentration and a longer reaction time, both the dimensional analysis and the EPD pattern (Fig. 4D and 5D) showed a larger crystalline domain size for the monoclinic phase, which still conserved a flat ellipsoid shape with average dimensions of 3.7 nm, 4.8 nm and 7.5 nm. Even under these conditions, the tetragonal phase did not exhibit a growth mechanism and the same size and shape reported for low precursor concentration and short reaction time were preserved. The detailed size and estimated standard deviation for each phase are reported in the ESI,<sup>†</sup> as well as the zirconia nanoparticles size obtained from TEM image analysis (Tables S2 and S3,<sup>†</sup> respectively).

These findings suggest that at the early stages of the synthesis, monoclinic and tetragonal particles are characterized to have a similar size and shape, and they are not distinguishable from each other from the TEM micrographs. A longer time and a higher precursor concentration only promoted the preferential orientation crystal growth of the monoclinic phase, which evolved into a flat ellipsoid shape easily identifiable from the TEM images. Furthermore, the Rietveld refinements of electron diffraction data were employed for the quantitative phase analysis of the ZrO<sub>2</sub> powders in order to determine the amount of monoclinic and tetragonal polymorphs. The results reported in Table 1 show the co-presence of both phases for each tested reaction condition, highlighting a higher monoclinic phase content for a longer reaction time and a higher concentration. To prove the accuracy of the Rietveld analysis, the *R*-factors and refined cell parameters for each sample were reported alongside.

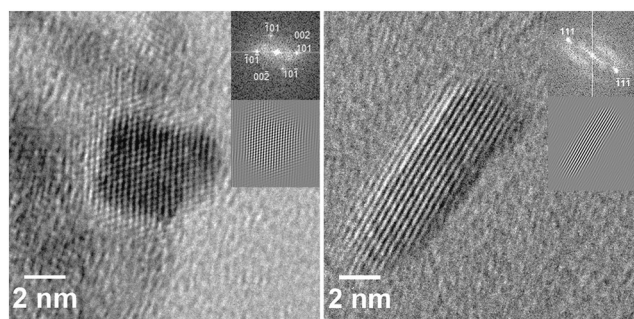
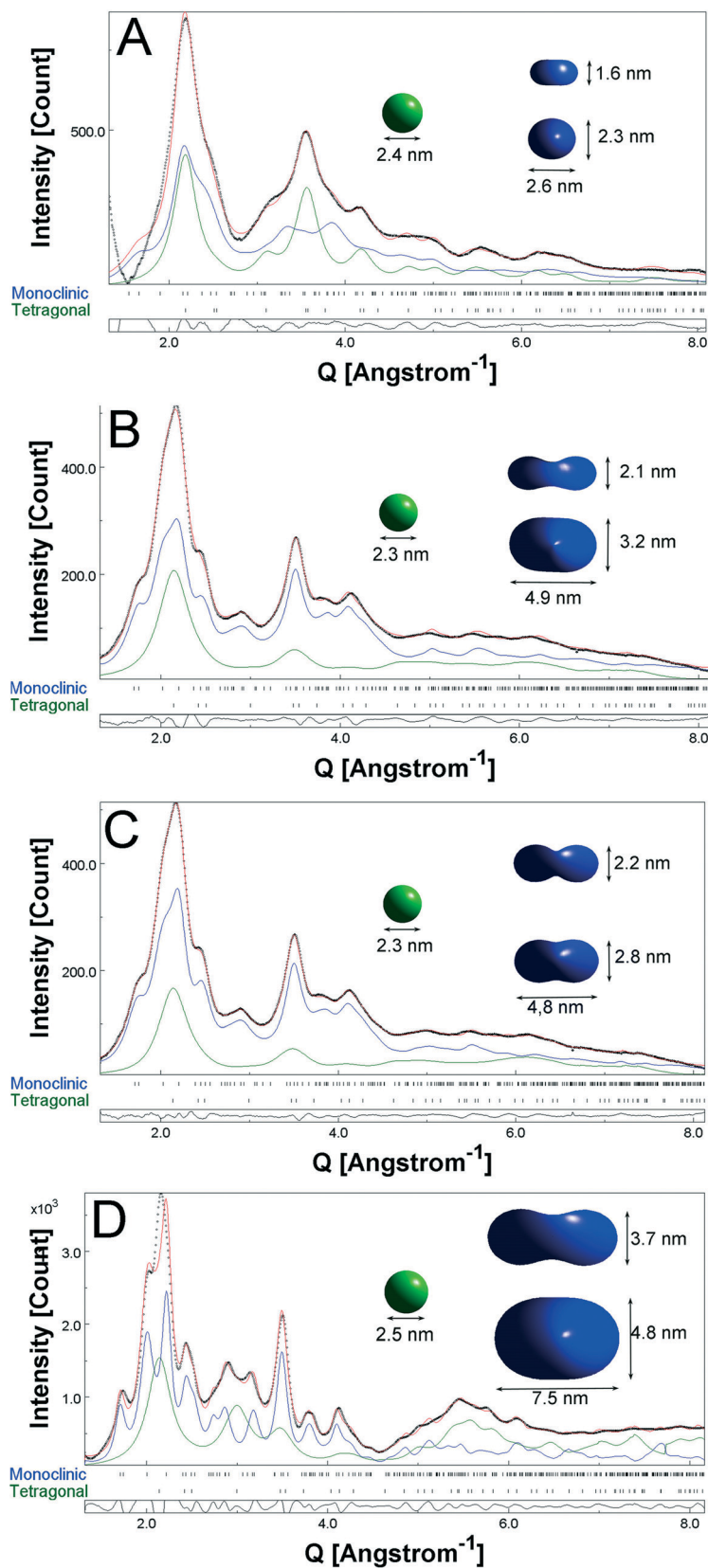


Fig. 3 On the left side a typical HR-TEM micrographs of a pseudo-spherical t-ZrO<sub>2</sub> particle viewed along [010], on the right side a typical HR-TEM micrographs of an elongated m-ZrO<sub>2</sub> particle viewed along [011]; in the insets are the corresponding indexed FFT pattern<sup>51</sup> (upper) and the filtered image (lower) of each micrograph.



**Fig. 4** Intensity diagrams and representative models of the nanocrystal shape and size (green for tetragonal and blue for monoclinic) extracted from the microstructural Rietveld analysis applied to the electron diffraction pattern of zirconia nanopowders: (A)  $0.16Z_{2.5}$ , (B)  $0.16Z_{2.4}$ , (C)  $0.5Z_{2.5}$ , and (D)  $0.5Z_{2.4}$ . Dot line in the intensity diagrams: experimental intensity profile; red line: calculated profile; green line: tetragonal intensity contribution; blue line: monoclinic intensity contribution. The lower part of each graph shows the difference between the experimental and calculated data.

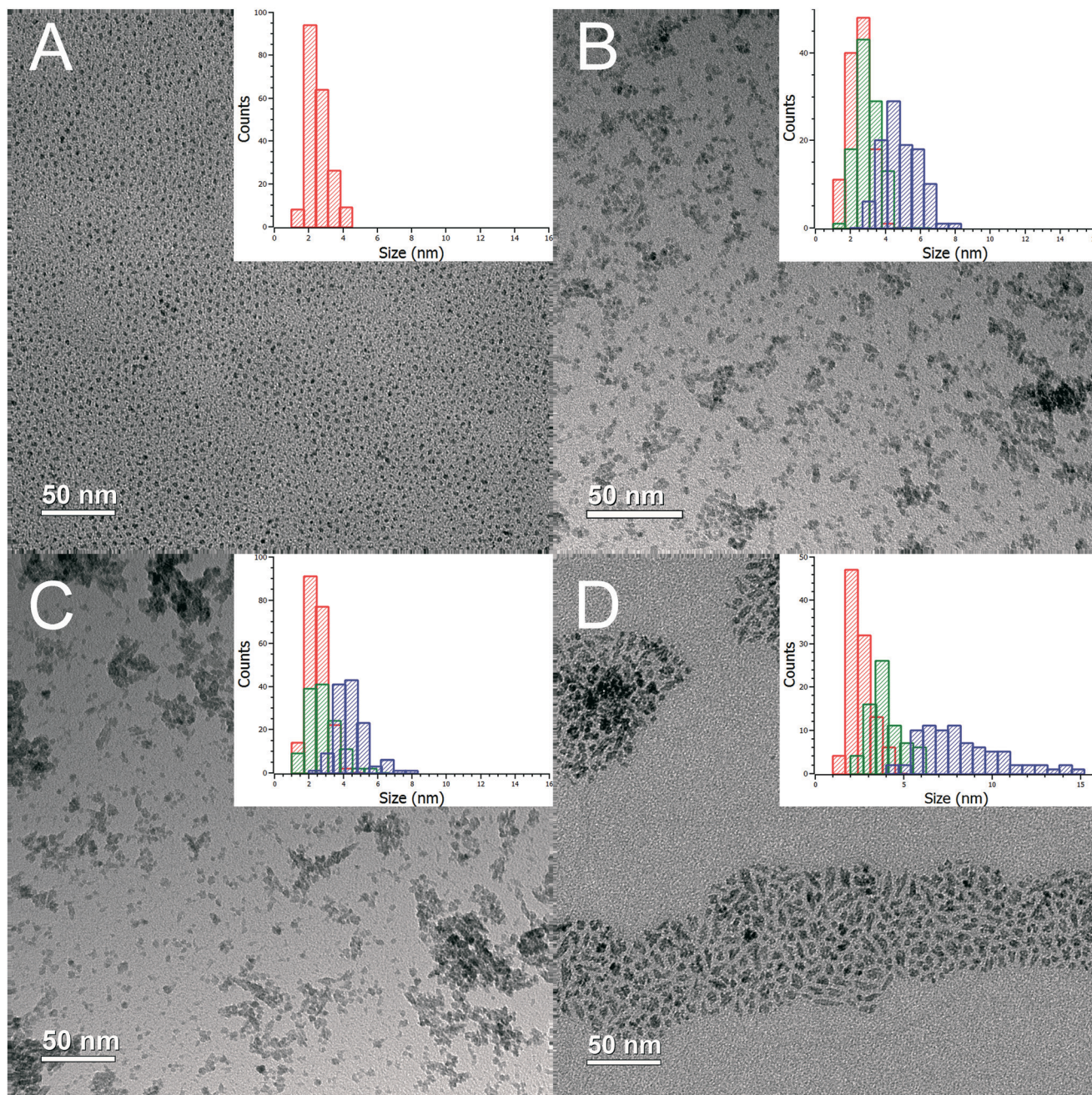


Fig. 5 Bright field TEM micrographs of the  $\text{ZrO}_2$  nanocrystals and their respective dimensional distribution graph at different monomer concentrations and reaction times: (A)  $0.16\text{Z}_{2.5}$ , (B)  $0.16\text{Z}_{24}$ , (C)  $0.5\text{Z}_{2.5}$ , and (D)  $0.5\text{Z}_{24}$ . Red column: diameter of the pseudo-spherical particles. Green column: short axis of the elongated particles. Blue column: long axis of the elongated particles.

## 4. Discussion

The reaction between metal halides and alcohols is undoubtedly among the most utilized methods for the non-aqueous synthesis of metal oxide nanoparticles, mainly due to the broad availability of reagents and the general advantages of using alcohols as non-toxic solvents.<sup>36</sup> Moreover, benzyl alcohol has been proven to be a powerful and versatile reaction system for non-aqueous synthesis of transition metals,<sup>54</sup> due to its capacity to direct particle growth, lead-

ing to low-dimensional particle morphologies and crystalline materials.

### Nanoparticle size and phase evolution

The reaction of  $\text{ZrCl}_4$  in  $\text{BzOH}$  for 7 hours yields a crystalline  $\text{ZrO}_2$  nanoparticle suspension.<sup>27</sup> Notably, the experimental parameters (*i.e.* concentration and reaction time) significantly affected the characteristics of the final powder. Generally, all samples appeared to be a mixture of tetragonal and

**Table 1** Rietveld analysis results of the electron powder diffraction pattern acquired on the zirconia nanostructured powders. The estimated standard deviations on the last digit for each refined parameter were reported in parentheses

Sample	Relative percentage of the crystalline phases		Refined cell parameters						<i>R</i> -Factor <i>R<sub>w</sub></i> (%)
			Tetragonal space group: <i>P42/nmc</i> :2		Monoclinic space group: <i>P121/c1</i>				
	t-ZrO <sub>2</sub> (%)	m-ZrO <sub>2</sub> (%)	<i>a</i> (Å)	<i>c</i> (Å)	<i>a</i> (Å)	<i>b</i> (Å)	<i>c</i> (Å)	$\beta$ (°)	
0.16Z <sub>2.5</sub>	66 (2)	44 (2)	3.534 (1)	5.207 (2)	5.130 (1)	5.194 (1)	5.294 (2)	98.62 (2)	2.01
0.16Z <sub>24</sub>	39 (3)	61 (3)	3.551 (2)	5.198 (2)	5.129 (2)	5.196 (2)	5.301 (2)	98.57 (2)	1.95
0.5Z <sub>2.5</sub>	49 (3)	51 (3)	3.567 (1)	5.190 (1)	5.137 (1)	5.181 (1)	5.298 (2)	98.71 (3)	1.82
0.5Z <sub>24</sub>	30 (2)	70 (3)	3.579 (1)	5.187 (2)	5.1401 (2)	5.184 (1)	5.306 (2)	99.02 (3)	2.48

monoclinic phases. This conclusion is in good agreement with our Raman and X-ray phase results. However, additional factors can be inferred from a more detailed data comparison. According to the XRD and Raman data (Fig. 1 and 2, respectively), as the reaction time elapsed (from 2.5 to 24 h), the amount of the monoclinic phase in the powders at the tested concentration (0.16 and 0.5 M) increased significantly. The increase in the monoclinic phase can be deduced from the rise of the monoclinic peaks in the XRD patterns (Fig. 1). However, pure m-ZrO<sub>2</sub> was never obtained, even at the longest reaction interval (24 h). This incomplete t → m transformation was attributed to the martensitic transformation of the zirconia powder<sup>9</sup> since it does not depend on time at a fixed temperature and only changes by varying the temperature. Noh *et al.*<sup>10</sup> observed the evolution of spherical tetragonal particles into long rod-like monoclinic particles as a result of the increase in the reaction temperature for the two different precursor mixtures. At a higher experimental temperature, the transformation into the monoclinic phase occurred.

It is well known that the monoclinic phase is the thermodynamically stable phase of zirconia from room temperature to 1170 °C. Nonetheless, even without the addition of stabilizing agents (*e.g.* divalent and trivalent cationic species such as Mg<sup>2+</sup>, Ca<sup>2+</sup>, Cr<sup>3+</sup>, and Y<sup>3+</sup>),<sup>55–57</sup> at some critical dimensions, a lower surface free energy allows the metastable tetragonal phase to grow. Specifically for nano-ZrO<sub>2</sub>, the role of the surface energy was first demonstrated by Garvie<sup>20</sup> with a predicted critical grain size of approximately 30 nm.

In this work, as the reaction time was extended, an increase in the particle size was observed by TEM (Fig. 5A–D) for both the 0.16 and 0.5 M samples justifying, in principle, the concurrent increase of monoclinic fraction amount. Nevertheless, the particles obtained were included within 3 nm

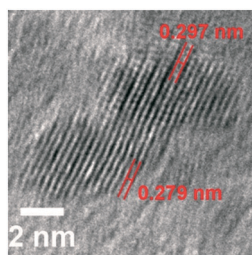


**Fig. 6** HRTEM image of zirconia powders 0.5Z<sub>7</sub> representing the merging of the zirconia monoclinic particle (bottom) and tetragonal particle (top).

for pseudo-spherical particles and within 8–10 nm (long axis) as the maximum length (Fig. 4 and 5), and the pure tetragonal phase was never observed. The occurrence of the mixed phase and even nearly pure monoclinic nanocrystalline zirconia with the predicted critical grain size is not the only parameter that dictates the phase evolution process of zirconia particles.<sup>33,58</sup> Guo *et al.* reported an even smaller monoclinic crystallite size in comparison with the tetragonal ones at the crystallization temperature.<sup>58</sup> Moreover, as it can be inferred from the TEM images (Fig. 5), no significant aggregation phenomena that may change the surface energy values (and consequently the critical grain size of metastable zirconia) affected the powder.<sup>18</sup> In the case of nano-zirconia, the presence of different anions such as OH<sup>-</sup>, Cl<sup>-</sup>, SO<sub>4</sub><sup>2-</sup>, and PO<sub>4</sub><sup>3-</sup>,<sup>59</sup> within the lattice or on the outer surface, were reported as possible elements that influence the t-ZrO<sub>2</sub> stabilization. Interestingly, the higher concentrated solution, 0.5 M, led to a higher amount of monoclinic zirconia in comparison with the 0.16 M samples (Table 1). The unexpected preferential growth of the monoclinic phase in the nanometric range is explained in the literature in terms of the twinning and/or lattice strain of the monoclinic crystallites or even due to different solubilities and chemical/physical factors in the process.<sup>58</sup> Since in this case the only difference is represented by the precursor concentration in solution, some effects on different particle surface stabilizations may be attributed to the variation of conditions in solution,<sup>60</sup> as well as the probable presence of HCl as reaction byproduct.<sup>27,35</sup>

### Nanoparticle morphological transformation

Interestingly, not only the size but also the morphology of the particles changed, (Fig. 3–5). Anisotropic particle growth was observed in different oxide and non-oxide nanoparticle syntheses<sup>61–63</sup> and in zirconia systems.<sup>9</sup> In addition, the latter possesses some peculiar characteristics connected to phase stability in the nanometric range. The crystalline phase features in relation to the particle nanomorphology can be inferred from Fig. 3 and 4. Just a few studies allow the correlation of changes in the ZrO<sub>2</sub> crystalline phase with its particle shape.<sup>10,33</sup> The morphology of a crystal is determined by relative specific surface energies associated with its facets.<sup>36</sup> If needed, the surface free energy of the nanocrystals can be modulated by introducing surfactants that adsorb onto the surfaces of growing crystallites.<sup>63</sup>

Tetragonal spheres and monoclinic rod-like particles were observed by introducing different suitable capping agents into reaction mixtures inducing preferential particle growth or by changing the experimental temperature. Nevertheless, in this synthesis, the time and precursor concentration played a role in the transformation. A similar result was reported by Stolzenburg *et al.*,<sup>64</sup> where the transition of the zirconia particle morphology from spherical to dendritic was observed, with increasing reaction time, while the concurrent monoclinic phase transformation occurred.

The evolution of growing nanocrystals in colloidal solutions is generally determined by the interplay of thermodynamic factors, such as the relative stability of crystal polymorphs, and kinetically limited processes, such as the diffusion of reactants.<sup>36</sup> As demonstrated by Shukla and Seal,<sup>18</sup> thermodynamics dictate the critical size for metastable tetragonal nanoparticles in an isolated, strain-free, ZrO<sub>2</sub> nanocrystal, which is reduced to 10 nm. Moreover, they suggested that similar to a liquid droplet on the solid surface, nanocrystals of that size must possess a spherical or near-spherical surface morphology in order to minimize their surface energy. The effectively small particle dimension of the 0.16Z<sub>2.5</sub> powder did not allow morphological evaluation of tetragonal and monoclinic particle. Nevertheless, despite the presence of some monoclinic impurities even in the pseudo-spherical 0.16Z<sub>2.5</sub> powder (Fig. 5A), this conclusion is confirmed by the HRTEM results and the TEM diffraction patterns (Fig. 3 and 4). An “optimized” near-spherical nanoscale morphology for the zirconia tetragonal phase was additionally identified by Barnard *et al.*<sup>65</sup> A computational model<sup>66</sup> presented the dependence of the global thermodynamic parameters on the total surface energy of the particle as a function of volume. The model describes the morphology of the nanomaterials on the basis of an expansion of the Gibbs free energy, taking into account the dimension and shape effects through the inclusion of the balance of surface energy as a function of exposed planes. Comparing this calculation with experimental results, Ribeiro *et al.*<sup>67</sup> found similar elements for titania and zirconia synthesized nanoparticles. The coalescence of smaller nanoparticles to form larger aggregates through the oriented attachment growth mechanism was proposed by the authors.

For this synthesis, evidence of particle coalescence has been observed by TEM (Fig. 6).

Also in this study, the nanocrystal growth mechanism was assumed to play an important role in the phase transformation. The growth itself may be mainly responsible for the tetragonal-to-monoclinic phase transformation.<sup>67</sup>

## 5. Conclusions

Phase, morphology and size evolution in zirconia nanoparticle crystallization was investigated at a constant temperature, by increasing the precursor concentration and reaction time with a non-aqueous synthesis in benzyl alcohol. No surface modifiers were added to the reaction mixture. By testing two different precursor concentrations, we revealed an increase in the monoclinic phase as a function of time.

Concurrently, an increase in the particle size was detected, and a simultaneous anisotropic zirconia particle growth was observed. This work offers a tool to design zirconia particles with anisotropic properties. Moreover, exploiting routinely and implemented characterization techniques, this work provides evidence that the evolution in size, morphology, and crystalline phase of zirconia nanoparticles can be directly related to synthesis variables under the described conditions. The presented Rietveld results indicate its potential as a thorough method for the characterization of crystalline nanomaterials in the near future. A clear understanding of the precise structure–function relationship is necessary to enable the preparation of highly controlled nanostructures. Answering the question to what extent does the growth mechanism contribute to the particle formation and their property evolution, together with the refinement of the existing characterization procedures, represents key steps towards a faster implementation of inorganic nanomaterials into technological applications.

## Conflicts of interest

There are no conflicts to declare.

## Acknowledgements

The authors would like to thank Mattia Ronchi for XRD measurements. F. V. acknowledges the Canada Foundation for Innovation (CFI) and the Ontario Ministry of Research and Innovation (MRI). LDN and FT acknowledge Accordo Quadro INSTM - Regione Lombardia (IT) for award “Sinatex”. LDN acknowledges Regione Lombardia (IT) for award “GRATA” (PON FESR 2014-2020, Asse I - Azione I.1.B.1.2).

## References

- 1 C. J. Murphy, T. K. Sau, A. M. Gole, C. J. Orendorff, J. Gao, L. Gou, S. E. Hunyadi and T. Li, *J. Phys. Chem. B*, 2005, 13857.
- 2 P. Prieel, H. A. Salami, R. H. Padilla, Z. Zhong and J. A. Lopez-Sanchez, *Chin. J. Catal.*, 2016, 37, 1619–1650.
- 3 A. P. Alivisatos, K. P. Johnsson, X. Peng, T. E. Wilson, C. J. Loweth, M. P. Bruchez and P. G. Schultz, *Nature*, 1996, 382, 609–611.
- 4 Y.-W. Lin, C.-W. Liu and H.-T. Chang, *Anal. Methods*, 2009, 1, 14–24.
- 5 N. Vasimalai and M. T. Fernandez-Arguelles, *Nanotechnology*, 2016, 27, 475505.
- 6 G. D. Willk, R. M. Wallace and J. M. Anthony, *J. Appl. Phys.*, 2001, 89, 5243–5275.
- 7 Z. Wang, Y. Lu, S. Yuan, L. Shi, Y. Zhao, M. Zhang and W. Deng, *J. Colloid Interface Sci.*, 2013, 396, 9–15.
- 8 A. Chen, Y. Zhou, S. Miao, Y. Li and W. Shen, *CrystEngComm*, 2016, 18, 580–587.
- 9 N. Zhao, D. Pan, W. Nie and X. Ji, *J. Am. Chem. Soc.*, 2006, 128, 10118–10124.
- 10 H.-J. Noh, D.-S. Seo, H. Kim and J.-K. Lee, *Mater. Lett.*, 2003, 57, 2425–2431.

- 11 M. Hartmanová, F. Kubel, V. Buršíková, E. E. Lomonova, J. P. Holgado, V. Navrátil, K. Navratil and F. Kundracik, *J. Phys. Chem. Solids*, 2008, **69**, 805–814.
- 12 W. Peng, G. R. Pickrell and A. Wang, *Opt. Eng.*, 2005, **44**, 124402.
- 13 A. G. Sato, D. P. Volanti, D. M. Meira, S. Damyanova, E. Longo and J. M. C. Bueno, *J. Catal.*, 2013, **307**, 1–17.
- 14 G. Wang, F. Meng, C. Ding, P. K. Chu and X. Liu, *Acta Biomater.*, 2010, **6**, 990–1000.
- 15 X.-J. Jin, *Curr. Opin. Solid State Mater. Sci.*, 2005, **9**, 313–318.
- 16 R. A. Muñoz, P. C. Cajas, J. E. Rodriguez, A. C. Rodrigues and C. R. M. Silva, in *Materials Science Forum*, Trans Tech Publ, 2014, vol. 798, pp. 145–153.
- 17 A. Navrotsky, *Proc. Natl. Acad. Sci. U. S. A.*, 2004, **101**, 12096–12101.
- 18 S. Shukla and S. Seal, *Int. Mater. Rev.*, 2005, **50**, 45–64.
- 19 R. C. Garvie, *J. Phys. Chem.*, 1965, **69**, 1238–1243.
- 20 R. C. Garvie, *J. Phys. Chem.*, 1978, **82**, 218–224.
- 21 C. Y. Tai, B.-Y. Hsiao and H.-Y. Chiu, *Colloids Surf., A*, 2004, **237**, 105–111.
- 22 S. Shukla, S. Seal and R. Vanfleet, *J. Sol-Gel Sci. Technol.*, 2003, **27**, 119–136.
- 23 F. Bondioli, A. M. Ferrari, C. Leonelli, C. Siligardi and G. C. Pellacani, *J. Am. Ceram. Soc.*, 2001, **84**, 2728–2730.
- 24 F. Bondioli, A. Bonamartini Corradi, A. M. Ferrari and C. Leonelli, *J. Am. Ceram. Soc.*, 2008, **91**, 3746–3748.
- 25 J. Joo, T. Yu, Y. W. Kim, H. M. Park, F. Wu, J. Z. Zhang and T. Hyeon, *J. Am. Chem. Soc.*, 2003, **125**, 6553–6557.
- 26 G. Garnweitner, L. M. Goldenberg, O. V. Sakhno, M. Antonietti, M. Niederberger and J. Stumpe, *Small*, 2007, **3**, 1626–1632.
- 27 F. Tana, M. Messori, D. Contini, A. Cigada, T. Valente, F. Variola, L. De Nardo and F. Bondioli, *Prog. Org. Coat.*, 2017, **103**, 60–68.
- 28 A. C. Dodd and P. G. McCormick, *J. Eur. Ceram. Soc.*, 2002, **22**, 1823–1829.
- 29 X. Feng, Y.-J. Bai, B. Lü, Y.-R. Zhao, J. Yang and J.-R. Chi, *J. Cryst. Growth*, 2004, **262**, 420–423.
- 30 J. Ding, T. Tsuzuki and P. G. McCormick, *Nanostruct. Mater.*, 1997, **8**, 75–81.
- 31 J. Polleux, A. Gurlo, N. Barsan, U. Weimar, M. Antonietti and M. Niederberger, *Angew. Chem.*, 2006, **118**, 267–271.
- 32 K. Sato, H. Abe and S. Ohara, *J. Am. Chem. Soc.*, 2010, **132**, 2538–2539.
- 33 X. Xu and X. Wang, *Nano Res.*, 2009, **2**, 891–902.
- 34 S. Acosta, R. Corriu, D. Leclercq, P. H. Mutin and A. Vioux, *J. Sol-Gel Sci. Technol.*, 1994, **2**, 25–28.
- 35 M. Niederberger and G. Garnweitner, *Chem. – Eur. J.*, 2006, **12**, 7282–7302.
- 36 M. Niederberger and N. Pinna, *Metal oxide nanoparticles in organic solvents: synthesis, formation, assembly and application*, Springer Science & Business Media, 2009.
- 37 D. Morselli, F. Bondioli, M. Fiorini and M. Messori, *J. Mater. Sci.*, 2012, **47**, 7003–7012.
- 38 D. Morselli, M. Niederberger, I. Bilecka and F. Bondioli, *J. Nanopart. Res.*, 2014, **16**, 2645.
- 39 L. Lutterotti, *Nucl. Instrum. Methods Phys. Res., Sect. B*, 2010, **268**, 334–340.
- 40 C. A. Schneider, W. S. Rasband and K. W. Eliceiri, *Nat. Methods*, 2012, **9**, 671–675.
- 41 L.-M. Peng, G. Ren, S. L. Dudarev and M. J. Whelan, *Acta Crystallogr., Sect. A: Found. Crystallogr.*, 1996, **52**, 257–276.
- 42 G. Ischia, H.-R. Wenk, L. Lutterotti and F. Berberich, *J. Appl. Crystallogr.*, 2005, **38**, 377–380.
- 43 L. Lutterotti, M. Bortolotti, G. Ischia, I. Lonardelli and H. R. Wenk, *Z. Kristallogr.*, 2007, **26**(Suppl), 125–130.
- 44 L. Lutterotti, R. Vasin and H.-R. Wenk, *Powder Diffr.*, 2014, **29**, 76–84.
- 45 J.-G. Kim, J. Seo, J.-W. Cheon and Y.-J. Kim, *Bull. Korean Chem. Soc.*, 2009, **30**, 183–187.
- 46 P. Boullay, L. Lutterotti, D. Chateigner and L. Sicard, *Acta Crystallogr., Sect. A: Found. Adv.*, 2014, **70**, 448–456.
- 47 D. A. Zyuzin, S. V. Cherepanova, E. M. Moroz, E. B. Burgina, V. A. Sadykov, V. G. Kostrovskii and V. A. Matyshak, *J. Solid State Chem.*, 2006, **179**, 2965–2971.
- 48 X. Tang and X. Zheng, *J. Mater. Sci. Technol.*, 2004, **20**, 485–489.
- 49 Q. Huang, W. Yuan, W. Huang, H. Cheng, Y. Zhou and H. Liu, *J. Sol-Gel Sci. Technol.*, 2015, **74**, 432–446.
- 50 T. Hirata, E. Asari and M. Kitajima, *J. Solid State Chem.*, 1994, **110**, 201–207.
- 51 M. Heidenreich, C. Kaps, A. Simon, F. Schulze-Küppers and S. Baumann, *Solid State Ionics*, 2015, **283**, 56–67.
- 52 J. Scola, X. Tassart, C. Vilar, F. Jomard, E. Dumas, Y. Veniaminova, P. Boullay and S. Gascoin, *J. Phys. D: Appl. Phys.*, 2015, **48**, 145302.
- 53 A. Serafini, L. Lutterotti, S. Gross and S. Gialanella, *Powder Diffr.*, 2017, **32**(S1), S63–S68.
- 54 M. Niederberger, M. H. Bartl and G. D. Stucky, *J. Am. Chem. Soc.*, 2002, **124**, 13642–13643.
- 55 D. L. Porter and A. H. Heuer, *J. Am. Ceram. Soc.*, 1979, **62**, 298–305.
- 56 R. C. Garvie, *J. Am. Ceram. Soc.*, 1968, **51**, 553–556.
- 57 C. Viazzi, J.-P. Bonino, F. Ansart and A. Barnabé, *J. Alloys Compd.*, 2008, **452**, 377–383.
- 58 G.-Y. Guo and Y.-L. Chen, *J. Solid State Chem.*, 2005, **178**, 1675–1682.
- 59 M. Skovgaard, K. Almdal and A. Van Lelieveld, *J. Mater. Sci.*, 2010, **45**, 6271–6274.
- 60 T. A. Cheema and G. Garnweitner, *CrystEngComm*, 2014, **16**, 3366–3375.
- 61 C. Pacholski, A. Kornowski and H. Weller, *Angew. Chem., Int. Ed.*, 2002, **41**, 1188–1191.
- 62 A. Chemseddine and T. Moritz, *Eur. J. Inorg. Chem.*, 1999, **1999**, 235–245.
- 63 X. Peng, L. Manna, W. Yang, J. Wickham, E. Scher, A. Kadavanich and A. P. Alivisatos, *Nature*, 2000, **404**, 59–61.
- 64 P. Stolzenburg, A. Freytag, N. C. Bigall and G. Garnweitner, *CrystEngComm*, 2016, **18**, 8396–8405.
- 65 A. S. Barnard, R. R. Yeredla and H. Xu, *Nanotechnology*, 2006, **17**, 3039.
- 66 A. S. Barnard and L. A. Curtiss, *Rev. Adv. Mater. Sci.*, 2005, **10**, 105–109.
- 67 C. Ribeiro, C. Vila, J. Milton Elias de Matos, J. Bettini, E. Longo and E. R. Leite, *Chem. – Eur. J.*, 2007, **13**, 5798–5803.